CMST 23(3) 185–198 (2017) DOI:10.12921/cmst.2017.00000012

Transient Heat Flow in a One-component Lennard-Jones/spline Fluid. A Non-equilibrium Molecular Dynamics Study

Bjørn Hafskjold

Department of Chemistry, Norwegian University of Science and Technology
N-7491 Trondheim, Norway
E-mail: bjorn.hafskjold@ntnu.no

Received: 20 February 2017; revised: 27 March 2017; accepted: 02 April 2017; published online: 09 September 2017

Abstract: A one-component Lennard-Jones/spline fluid at equilibrium was perturbed by a sudden change of the temperature at one of the system's boundaries. The system's response was determined by non-equilibrium molecular dynamics (NEMD). The results show that heat was transported by two mechanisms: (1) Heat diffusion and conduction, and (2) energy dissipation associated with the propagation of a pressure (shock) wave. These two processes occur at different time scales, which makes it possible to separate them in one single NEMD run. The system was studied in gas, liquid, and supercritical states with various forms and strengths of the thermal perturbation. Near the heat source, heat was transported according to the transient heat equation. In addition, there was a much faster heat transport, correlated with a pressure wave. This second mechanism was similar to the thermo-mechanical "piston effect" in near-critical fluids and could not be explained by the Joule-Thomson effect. For strong perturbations, the pressure wave travelled faster than the speed of sound, turning it into a shock wave. The system's local measurable heat flux was found to be consistent with Fourier's law near the heat source, but not in the wake of the shock. The NEMD results were, however, consistent with the Cattaneo-Vernotte model. The system was found to be in local equilibrium in the transient phase, even with very strong perturbations, except for a low-density gas. For dense systems, we did not find that the local equilibrium assumption used in classical irreversible thermodynamics is inconsistent with the Cattaneo-Vernotte model.

Key words: transient heat flow, molecular dynamics, Joule-Thomson effect, fluids, shock waves, piston effect

I. INTRODUCTION

Approximately two decades after Alder and Wainwright had published their pioneering work on molecular dynamics simulations [1], Hoover and co-workers explored the applications of this new scientific tool to strongly non-equilibrium processes [2]. The reason for shear thinning in viscous flow, the thickness of a shock wave in dense fluids, and the limits of linear flow theories were open questions at the time. This initiated a new line of computer simulation applications that proved to be very important in the understanding of fluid flow.

Explosions, collisions of solid bodies, rapid phase transitions, volcanic eruptions, supersonic shocks, and sudden local heating are examples of processes that generate shock waves. Some examples of rapid phase transitions are contact between molten metal and water in the metallurgical industry [3], steam explosions in nuclear reactors [4], and spills of liquefied natural gas on soil or water [5]. Such accidents may cause shockwaves of concern with respect to safety. Shock compression has for decades been used to study the kinetics of rapid chemical reactions [6] and material properties and fracturing of solids [7]. There is a vast literature on the topic, including the excellent books by Landau and Lifshitz [8], Hirschfelder et. al. [9], and Hoover and Hoover [10], and there are conference series devoted to shock waves.

Naturally, most of the literature on shock waves relate to gases. Analyses are based on hydrodynamics and numerical solution of the Navier-Stokes equations. On the other hand, the simulation work of Hoover [2] and subsequent work [11, 12, 13, 14] have explored the properties of liquids and solids. Brad Lee Holian, another pioneer in the field, wrote an interesting and quite personal review on computer simulations of

shock waves in 1993 [15]. A few recent examples that illustrate some of the current topics of interest, are the studies of local equilibrium properties (or rather the lack of equilibrium) in an ideal-gas shock wave [16], shock wave compression and its relation to the Joule-Thomson effect [14], and phonon transport at very short time scales [17].

In most of the reported atomistic simulations of shock waves, the shock is generated by a piston on one side of the system. The coordinate system is chosen to move with the shock front, making the shock wave stationary in these coordinates [18]. The properties of the shock wave is typically analysed in terms of the Rankine-Hugoniot conditions in a Lagrangian framework [19, 20].

A shock wave is a highly non-equilibrium phenomenon. It has been clearly demonstrated that local fluid properties, such as the temperature and pressure, deviate from the equilibrium properties in the shock wave, especially for two-dimensional systems at low density [16]. This is illustrated by *e.g.* a non-isotropic kinetic temperature in a control volume of size corresponding to a fluid particle mean free path.

In compressible fluids, and especially in near-critical fluids, it has been shown that thermal equilibration in a locally heated fluid occurs faster than expected from diffusion of heat as described by the heat equation,

$$\frac{\partial T}{\partial t} = \alpha \nabla^2 T \tag{1}$$

where T is temperature, t is time, α is the thermal diffusivity, *i. e.* the thermal conductivity divided by density and constant-pressure heat capacity, and ∇^2 is the Laplace operator. This fast heating is the so-called "critical speeding-up" or "piston effect" [21, 22]. The phenomenon of critical speeding-up was not fully understood until Onuki *et. al.* [23] explained it in terms of the connection between entropy-, pressure-, and thermal changes in the fluid. Whereas heat diffusion in a closed container has a characteristic time $\tau_{\mathrm{D}} = L^2/\alpha$, where L is the length of the container, a typical time scale for the piston effect is $\tau_{\mathrm{PE}} = \tau_{\mathrm{D}}/(\gamma - 1)^2$, where γ is the ratio between the heat capacity at constant pressure and constant volume. The divergence of γ in the near-critical region of the phase diagram gives the "critical speeding-up" of thermal equilibration. Even though the thermodynamic states considered in this paper are not "near critical", the closest case show as an example $\tau^*_{\mathrm{D}} \sim 17\,000$ and $\tau^*_{\mathrm{PE}} \sim 3\,000$, *i. e.* a factor roughly 3 between the two time constants.

The questions discussed in this paper are limited to observations of heat diffusion and the piston effect on an atomistic scale. The pressure- and temperature waves were generated with a local heat source acting by rescaling the particles' kinetic energy. The heat was suddenly turned on in an equilibrated fluid system. Although the results are in qualitative agreement with the hydrodynamics literature, a more detailed analysis in terms of the theory behind the piston effect and the system's entropy production is deferred to a later paper because we are lacking information about the system's viscosity.

This work differs from previously reported simulations in that the perturbation was isotropic rather than a directed pulse. The system's response was studied in an Eulerian framework with boundary-driven non-equilibrium molecular dynamics simulations (NEMD) as described by Ikeshoji and Hafskjold [24]. The following questions were addressed:

1. When the heat source is suddenly switched on, it generates a pressure increase near the heat source (like an explosion), a pressure (shock) wave, a local gas compression, and a local heating effect accompanying the pressure wave. What is the relation between the pressure wave and the heat wave?
2. Do the temperature gradients near the heat source and around the pressure wave give rise to a heat flux that may be described by Fourier's law?
3. The Cattaneo-Vernotte model for heat transfer [25, 26] introduces the concept of a thermodynamic relaxation time and may be considered as a generalization of Fourier's law [27]. How well does this model apply to the transient situation?
4. Is local equilibrium, in the sense that local thermodynamic properties in the irreversible process are given by the (equilibrium) equation of state, fulfilled with this method for heat- and pressure shock wave generation?

In Section 2, we give a brief account on the details of the simulations. We should emphasize here that the thermodynamic states used in this work are supercritical, but not near critical in the usual sense; the temperatures are more than 10 % above the system's critical temperature. The results are presented and discussed in Section 3. The somewhat surprising results in light of most of the previous NEMD studies are briefly discussed in Section 4, and tentative conclusions are given in Section 5.

II. SIMULATIONS AND BASIS FOR DATA ANALYSIS

The system of concern in this work is a one-component, 3D Lennard-Jones/spline (LJ/s) model defined by the pair potential [28]

$$u(r) = \begin{cases} 4\epsilon\left[\left(\frac{\sigma}{r}\right)^{12} - \left(\frac{\sigma}{r}\right)^{6}\right] & \text{for } r \le r_s \\ a(r - r_c)^2 + b(r - r_c)^3 & \text{for } r_s \le r \le r_c \\ 0 & \text{for } r \ge r_c \end{cases} \tag{2}$$

The parameters ϵ and σ are the usual LJ parameters. The parameters r_s, r_c, a, and b are determined so that the potential and its derivative (the force) are continuous at $r = r_s$ (the inflection point of the LJ potential) and $r = r_c$ (the cut-off distance). This leads to

Tab. 1. Definitions of reduced variables used in this work

Property	Definition
Temperature	$T^* = \frac{k_\mathrm{B}T}{\epsilon}$
Density	$n^* = \frac{N\sigma^3}{V}$
Pressure	$P^* = \frac{P\sigma^3}{\epsilon}$
Time	$t^* = \frac{t}{\sigma}\left(\frac{\epsilon}{m}\right)^{1/2}$
Length	$x^* = \frac{x}{\sigma}$
Velocity	$v^* = v\left(\frac{m}{\epsilon}\right)^{1/2}$
Mass flux	$J_\mathrm{m}^* = J_\mathrm{m}\frac{\sigma^3}{m}\left(\frac{m}{\epsilon}\right)^{1/2}$
Energy flux	$J_\mathrm{energy}^* = J_\mathrm{energy}\frac{\sigma^3}{m}\left(\frac{m}{\epsilon}\right)^{1/2}$
Measurable heat flux	$J_\mathrm{q}^* = J_\mathrm{q}\frac{\sigma^3}{m}\left(\frac{m}{\epsilon}\right)^{1/2}$

$$r_s = \left(\frac{26}{7}\right)^{1/6}\sigma \approx 1.24\sigma \tag{3a}$$

$$r_c = \frac{67}{48}r_s \approx 1.74\sigma \tag{3b}$$

$$a = -\frac{24192}{3211}\frac{\epsilon}{r_s^2} \tag{3c}$$

and

$$b = -\frac{387072}{61009}\frac{\epsilon}{r_s^3}. \tag{3d}$$

This definition of the spline makes the potential convenient to work with because (1) it is unambiguous (no additional need to specify cut-off, shift, or smoothing function), (2) no correction for long-range tail is necessary[1], and (3) the potential is of shorter range than typical LJ potentials, which has cut-off typically at $r_c/\sigma = 2.5 - 3.5$. The last feature makes the MD code run about twice as fast as with the LJ potential. The LJ/s potential contains essentially the same physics as the LJ potential. In particular, the fluid structure, which is dominated by the repulsive forces, is essentially the same as for the full LJ potential, whereas the thermodynamic properties are significantly different. For instance, the critical temperature of the LJ model is $T_\mathrm{c}^* \cong 1.33$ [29], whereas the LJ/s model has $T_\mathrm{c}^* \approx 0.9$ [unpublished data].

Throughout this paper, numerical values are reported in the usual LJ units when the symbols are marked with an asterisk. The definitions of the reduced variables are shown in Tab. 1.

A boundary-driven NEMD method as described by Ikeshoji and Hafskjold [24] and by Hafskjold *et. al.* [30] was used, except that the HEX algorithm was replaced by thermostats in the layers used for supply and withdrawal of kinetic energy.

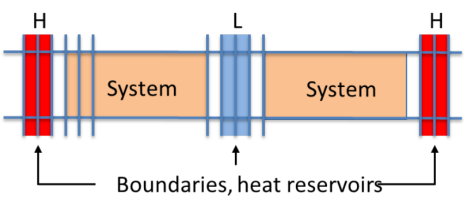

Fig. 1. NEMD cell layout. See text for explanation

A sketch of the NEMD cell layout is shown in Fig. 1. The cell was non-cubic with an aspect ratio L_x:L_y=L_x:L_z= 32 with periodic boundary conditions in all three directions. The cell was divided into 128 layers of equal thickness perpendicular to the *x*-direction (the direction of the transport processes). One layer at each end was thermostatted to a temperature T_H and the two layers in the center of the cell were thermostatted

[1] This means that the model does not pretend to be the full LJ model, it is just a convenient alternative.

Tab. 2. Summary of simulation conditions. In all cases, $T_H^* = 10.0$

Run no.	n^*_{overall}	T^*_{L}	t^*_{run}	$\triangle t^*$	P^*_{eq}	$Z = (PV)/(Nk_{\mathrm{B}}T)$	Comment
1	0.8	1.0	400	8.0	2.36±0.02	2.95±0.02	
2	0.8	1.0	20	0.4	2.36±0.06	2.95±0.02	
3	0.4	1.0	100	2.0	0.169±0.008	0.42±0.02	
4	0.4	1.0	100	2.0	0.169±0.008	0.42±0.02	(1)
5	0.4	1.0	10	0.2	0.17±0.02	0.43±0.05	(2)
6	0.4	1.0	10	0.2	0.17±0.04	0.4±0.1	(2,3)
7	0.4	1.0	5	0.1	0.17±0.02	0.43±0.05	(2)
8	0.4	3.0	100	2.0	1.86±0.03	1.55±0.03	(4)
9	0.02	1.0	400	4.0	0.0189±0.0003	0.95±0.02	
10	0.001	1.0	600	4.0, 2.0	$9.98\times10^{-4}\pm7\times10^{-6}$	1.000±0.007	(5)

1. Pulsed heat source, length of pulse was 4 in LJ units
2. Started from run 3 at $t^* = 60$.
3. With layer thickness $\triangle x^* = 1.35$
4. Test of Joule-Thomson effect on heat pulse
5. $\triangle t^* = 4.0$ until $t^* = 400$, $\triangle t^* = 2.0$ thereafter

to a temperature T_{L}. The thermostats used a simple velocity rescaling algorithm with local momentum control,

$$\mathbf{v}_i^{\mathrm{new}} = a\mathbf{v}_i^{\mathrm{old}} + \boldsymbol{\beta} \tag{4}$$

where $\mathbf{v}_i^{\mathrm{old}}$ and $\mathbf{v}_i^{\mathrm{new}}$ are the velocity of particle *i* before and after the scaling, respectively. Details of the thermostatting algorithm are presented in Appendix A. The thermostat in the hot layers was independently applied to the *x*-, *y*-, and *z*-components of the velocities. Otherwise, the temperature in the hot layers developed a non-isotropic profile due to energy loss in the *x*-direction.

The Velocity Verlet algorithm was used to integrate the equations of motion.

The regions marked "System" in Fig. 1, not including the thermostatted layers, were used for acquiring thermodynamic properties and transport data. The mirror symmetry of the system was used to pool data from the left and right sides of the cold layers.

The transient simulations were done with $N = 128,000$ particles, so each layer contained 1000 particles on average, except that the dilute-gas case was done with $N = 432,000$. Further details of the simulations are given in Tab. 2.

The phase diagram of the 3D LJ/s system shows gas, liquid, and solid phases with a critical temperature $T_{\mathrm{c}}^* \approx 0.9$ in reduced LJ units, a critical number density $n_c^* \approx 0.4$, and a triple-point temperature $T_{\mathrm{tp}}^* \approx 0.5$. Four transient states were studied in this work, at overall densities $n^* = 0.001$ (dilute gas), 0.02 (dense gas), 0.4 (supercritical), and 0.8 (liquid).

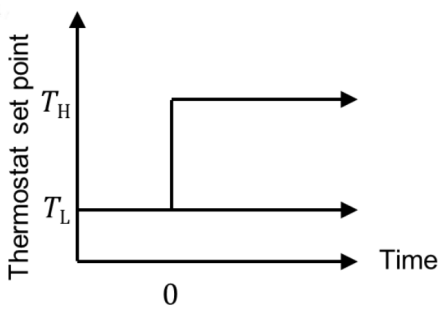

Fig. 2. Generation of transient states by suddenly increasing the temperature in the hot layers

Prior to the transient simulations, the system was equilibrated at a uniform (supercritical) temperature $T^* = 1.0$. At time zero, the thermostat set point in the hot layers was

Tab. 3. Parameters used for computation of local averages in space. The mean free path λ^* as computed from elementary kinetic theory is included for comparison with the layer thickness $\triangle x^*$. The thermal diffusivity, α^*, was determined as described in Section 3.2. See also footnotes to Tab. 2

Case	n^*_{overall}	$\triangle x^*$	L_x^*	L_y^*, L_z^*	λ^*	α^*
Liquid	0.8	4.28	545.2	17.04	0.28	3.5
Supercritical	0.4	5.39	686.6	21.46	0.56	6.9
Dense gas	0.02	14.62	1862	58.20	11.25	56
Dilute gas	0.001	59.53	7620	238.1	225.1	-

suddenly set to $T_{\rm H}^* = 10.0$ and maintained at that value as shown in Fig. 2, while the cold layers were kept at $T_{\rm L}^* = 1.0$. The system's response was monitored from then on. The system in all the other layers was free to adjust its properties according to the impact from the hot layers.

In one case, the thermostats were set $T_{\rm H}^* = 10.0$ and $T_{\rm L}^* = 3.0$, starting from equilibrium at $T^* = 3.0$ and $n^* = 0.4$ in order to examine the cause of the observed heat wave (see Section 3.2). A pulsed heat source was also used (run 4) without giving significantly different results from those reported here, as shown in Section 3.2.

In order to estimate the magnitude of random errors in the transient phase, 20 runs were started from different equilibrium configurations, generated by initial Monte Carlo sequences of different lengths at $T^* = 10.0$, then cooled down at constant density to $T^* = 1.0$ and allowed to equilibrate with equilibrium MD. The MD time step was in all cases $\delta t^* = 0.002$. A summary of the simulation conditions are listed in Tab. 3.

Instantaneous values for the properties of interest were acquired for each layer every 20 time step and accumulated for computation of averages over time intervals $\triangle t^*$ to obtain local properties. The values of $\triangle t^*$ are given in Tab. 2.

Some characteristic geometric data for the simulation cell are given in Tab. 3. For comparison, the mean free path λ^* as computed from elementary kinetic theory is also given in the table.

The instantaneous, local kinetic temperature in a control volume (layer) CV was computed as

$$T_{\rm CV} = \frac{m}{3N_{\rm CV}k_{\rm B}} \sum_{i\in{\rm CV}} (\mathbf{v}_i - \mathbf{v}_{\rm cm})^2, \tag{5}$$

where m is the mass of each particle, $N_{\rm CV}$ is the instantaneous number of particles in the control volume,[2] $\mathbf{v}_i$ is the instantaneous velocity of particle i, and $k_{\rm B}$ is Boltzmann's constant. Note that $\mathbf{v}_{\rm cm}$ is the local centre-of-mass velocity averaged over the time interval $\triangle t$. The velocities refer to the MD cell frame of reference. Assuming small relative fluctuations in $N_{\rm CV}$, the average kinetic temperature may be expressed as

$$\overline{T_{\rm CV}} = \frac{1}{3k_B}\left[2\overline{ke} - \frac{1}{m}\left(\frac{\overline{J_m}}{\overline{n}}\right)^2\right] (6) \tag{6}$$

where ke is the kinetic energy per particle and J_m is the mass flux in the MD cell frame of reference,

$$J_m = \frac{m}{V_{\rm CV}} \sum_{i\in{\rm CV}} \mathbf{v}_i, \tag{7}$$

where $V_{\rm CV}$ is the size of the control volume. The bars in Eq. (6) denote time averages over the interval $\triangle t$. The computation of the kinetic temperature was done during postprocessing of the raw MD data because $\mathbf{v}_{\rm cm}$ was not computed on the run.

In our analysis of the pressure- and heat waves, we shall also need the heat flux. The heat flux that is readily obtained in boundary-driven-NEMD is the *energy flux*, also called the *total heat flux* [31]. The energy flux $J_{\rm energy}^{\rm MD}$ is given in the MD cell frame of reference as [32]

$$J_{\rm energy}^{\rm MD} = \frac{1}{V_{\rm CV}} \sum_{i\in{\rm CV}} \left[e_i\mathbf{v}_i - \frac{1}{2}\sum_{j=1}^{N} [\mathbf{v}_i \cdot \mathbf{F}_{ij}]\mathbf{r}_{ij} \right], \tag{8}$$

where e_i is the sum of potential and kinetic energy of particle i, $\mathbf{F}_{ij}$ is the force acting on i due to j, and $\mathbf{r}_{ij}$ is the vector from the position of i to the position of j. The heat flux related to Fourier's law is the *measurable heat flux*, which excludes the transported heat due to the fluid flow (or center-of-mass velocity). The measurable heat flux is [32]

$$J_{\rm q} = \frac{1}{V} \sum_{i\in{\rm CV}} \left[e_i\left(\mathbf{v}_i - \mathbf{v}_{\rm cm}\right) - \frac{1}{2}\sum_{j=1}^{N} [(\mathbf{v}_i - \mathbf{v}_{\rm cm}) \cdot \mathbf{F}_{ij}]\mathbf{r}_{ij} \right] \tag{9}$$

It is not straightforward to compute the transient heat flux in boundary-driven NEMD from this expression because the center-of-mass velocity is unknown at the time of the computation. The computation of $J_{\rm q}$ is therefore done in the postprocessing, like for the kinetic temperature. The measurable heat flux is independent of the frame of reference and may be expressed as

$$J_{\rm q} = J_{\rm energy}^{\rm MD} - J_m H, \tag{10}$$

where H is the local enthalpy [31]. Both fluxes on the rhs of Eq. (10) relate to the MD cell frame of reference, and H is a property of the fluid.[3] Eq. (10) provides a convenient way to compute the measurable heat flux in NEMD.

III. RESULTS

III. 1. The shock wave

The sudden increase in the hot-layer temperature generated a pressure wave in the system. Run no. 1 was chosen long enough so that the wave could move until it hit the wave coming from the opposite end of the MD cell, was reflected and moved back and forth until the system eventually reached a state close to steady state with a more uniform pressure. The illustration in Fig. 3 is for the liquid case. This behaviour is consistent with what has been found from numerical solution of the governing balance equations with a finite elements

[2] In reduced units $V_{\rm CV}^* = \triangle x^* L_y^* L_z^*$, where $\triangle x^*$ is the thickness of each layer as listed in Tab. 3.

[3] The enthalpy has an ideal-gas contribution that depends on the temperature. The kinetic temperature given by Eq. (6), corrected for the center-of-mass velocity, must be used here. The correction has nothing to do with the frame of reference, but is a consequence of the definition of the kinetic temperature.

method or numerical inversion of their Laplace transforms for compressible fluids, see *e.g.* refs. [33] and [34].

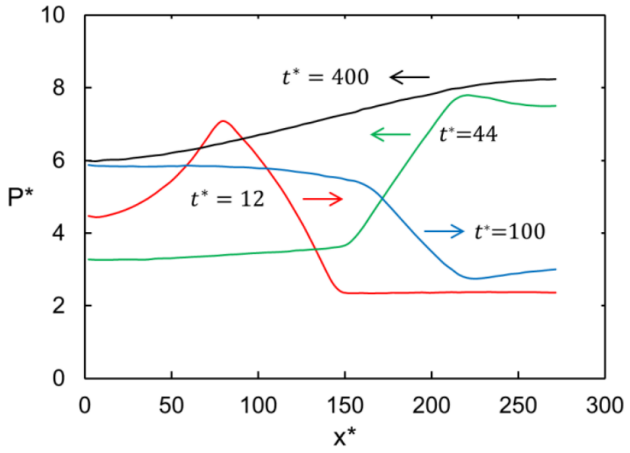

Fig. 3. Results from run 1 showing pressure waves moving back and forth in the MD cell. The distance from the hot end of the MD cell is x^* (in LJ units). The arrows indicate the direction of the wave motion. The system had not yet reached stationary state at the end of the run ($t^* = 400$). The shock front is artificially wide because it is smoothed by the large time interval used for computing averages, $\triangle t^* = 8$, in this case. During this time, the wave had moved a distance approximately 70 in LJ units

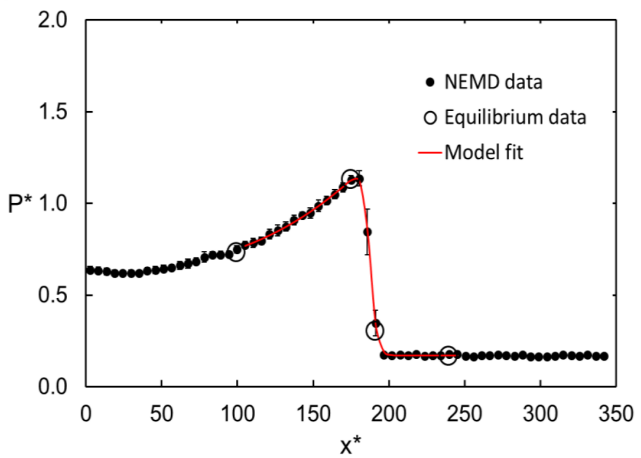

Fig. 4. Pressure profile for run 3 at time $t^* = 50$ after the heat was turned on with $T_H^* = 10.0$. The uncertainties are shown as three standard deviations of the mean of 20 independent runs with different initial configurations. The four large circles are equilibrium values, see Section 3.4. The red line is a model fit used to determine the peak of the pressure wave

The length of runs 2 – 10 was chosen so that the shock wave just reached the centre of the MD cell at the end of the run. Disturbance from the reflected wave was thus avoided and the system behaved like a semi-infinite system during this time. The low-temperature thermostat actually had no effect for these runs. Shorter time intervals were used in these cases, see Tab. 2. As an example, Fig. 4 shows the pressure profile in the supercritical fluid some time after the heat is turned on in run 3, at $t^* = 50$. As the wave progresses, it loses energy, slows down (see Fig. 6) and its amplitude is damped.

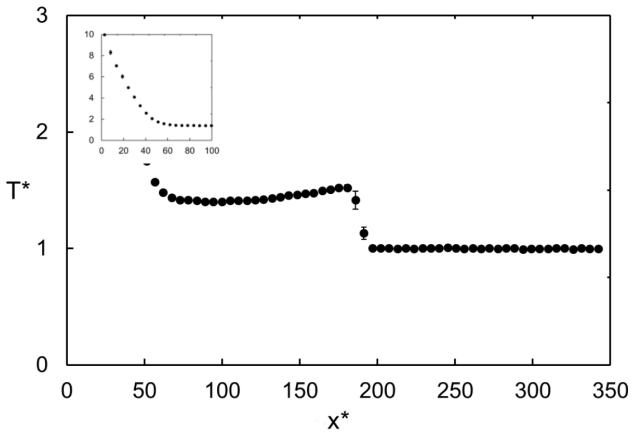

Fig. 5. Temperature profile at the same condition as shown in Fig. 4. The insert shows the temperature profile near the hot source. Comparing Figs. 4 and 5 shows that the temperature wave is synchronous with the pressure wave

The corresponding temperature profile shown in Fig. 5 also shows a shock-wave behaviour in addition to the expected diffusion of heat near the hot layer (at $x^* = 0$). The thermal diffusivity of the fluid was determined from the temporal evolution of the temperature profile near the hot layer (insert in the Fig. 5), see Section 3.2.

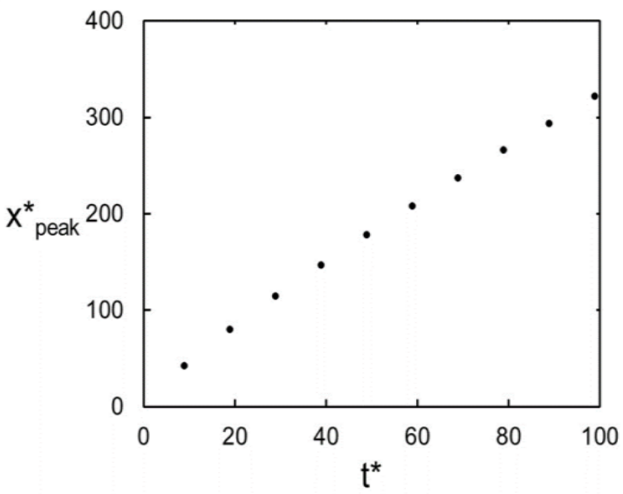

Fig. 6. Position of the pressure peak as function of time for the supercritical state. The slope is the travelling speed of the shock

The pressure- and temperature waves travelled with an almost constant speed. Fig. 6 shows the position of the pressure peak as function of time for run 3. The position of the peak was determined from a fit of the function

$$f(x) = a + b\frac{1 + c\left(\dfrac{x}{x_0}\right)^d}{1 + \left(\dfrac{x}{x_0}\right)^e}, \qquad (11)$$

where $a - e$ and x_0 are adjustable parameters determined with a least-squares method. An example of the fit is shown in Fig. 4. This function does not have a physical meaning, is was just used as a convenient model to determine the peak position by setting $f'(x) = 0$.

The thickness of the shock wave can be estimated from the data shown in Fig. 4. An approximate value is 15 LJ units. This is larger than the distance travelled by the wave during the time $\triangle t^*$ used for time averages, so the effect of smoothing shown in Fig. 3 is reduced or eliminated. In order to further check the smoothing effect of averaging in time and space, three additional runs, no. 5, 6, and 7 were made with finer resolutions, see Tab. 2. A comparison between data from runs 3 and 7 for $t^* = 64$ is shown in Fig. 7. For the values of $\triangle t^*$ used here, there is no effect of the time resolution, and the observed thickness of the pressure wave must be interpreted as representing the nature of the wave. The thickness of the wave front was found to be approximately 15 LJ units for the supercritical case.

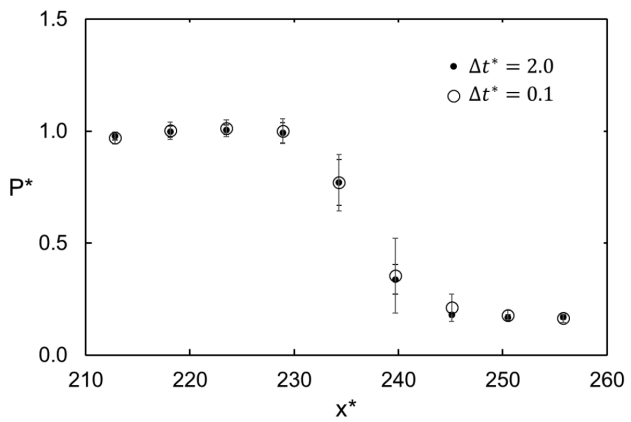

Fig. 7. Details of the shock wave for two time resolutions. Data from runs 3 and 7 for $t^* = 64$

Results for the liquid and dense gas cases show qualitatively the same shock-wave behaviour, but the ideal-gas case was different (see Section 3.4).

The slope of the curve in Fig. 6 decreases slightly with time, but the average over the range shown is $\partial x^*/\partial t^* \approx 3.1$ for the supercritical case. This should compare with the speed of sound, given by

$$v_s^2 = \frac{C_P}{C_V}\left(\frac{\partial P}{\partial n}\right)_T \qquad (12)$$

The properties on the rhs of Eq. (12) were computed from equilibrium MD simulations, see Appendix B for details. For the case shown in Fig. 4, the value was found to be $v_s^* \approx 1.5$ in front of the shock wave, *i.e.* the shock wave travelled with a Mach number approximately equal to 2. Similar results were found for the other dense cases, but the shock-like behaviour was softened as the density was reduced.

III. 2. Local heating

The temperature profile shown in Fig. 5 has two distinct features; (1) heat diffusion near the heat source and (2) a heat wave travelling syncronously with the pressure wave. The heat diffuses in the range between the heat source and the pressure wave. Using the case shown in Fig. 5 as an example, this range is approximately $0 < x^* < 100$ (see the figure insert). This range may be considered semi-infinite for $0 < t^* < 50$. With initial conditions $T(x,0) = T_i$ and boundary conditions $T(0,t) = T_{\rm H}$, $t > 0$, and $T(x \to \infty, t) = T_i$, the solution of the heat equation,

$$\frac{\partial T(x,t)}{dt} = \alpha \frac{\partial^2 T(x,t)}{\partial x^2} \qquad (13)$$

where α is the thermal diffusivity, is

$$T(x,t) = T_i + (T_{\rm H} - T_i)\ erfc\left(\frac{x}{2\sqrt{\alpha t}}\right) \qquad (14)$$

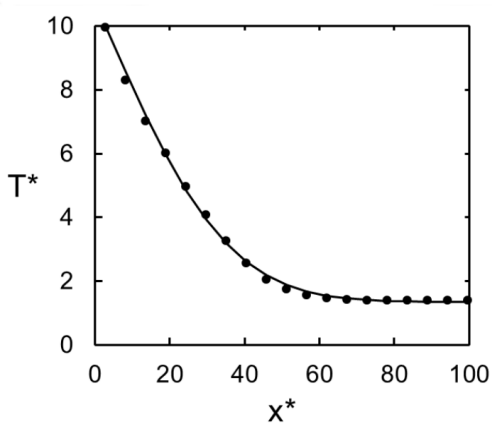

Fig. 8. Comparison of NEMD data (black circles) and model (line) for the case shown in Fig. 5 ($t^* = 50$). The model is a fit of Eq. (14) to the NEMD data

Note that the initial condition is $T_i = T_{\rm L}$, but the temperature does not fall back to $T_{\rm L}$ behind the heat wave. Therefore, the model, Eq. (14), was fitted to the NEMD data with the least squares method, using T_i as well as α as adjustable parameters, giving the fit shown in Fig. 8. Estimates for α^* are included in Tab. 3, except that a reliable value was not found for the dilute-gas case. The estimates may be used to check the consistency with the shock-wave properties as discussed in Section 3.3.

Although the NEMD data for $T\,(x,t)$ over a range of t allow for a more extensive analysis in terms of the heat equation, we shall leave this analysis by just noting that the model, Eq. (14), fits the NEMD data well with a constant thermal diffusivity over a very wide temperature range.

Turning to the region of the pressure- and heat waves, it should first be pointed out that the present simulation setup is quite different from most other MD studies. In this work, the pressure pulse is generated by increasing the particles' velocities in all directions, not only in the wave's travelling direction. Secondly, the particles' Maxwellian velocity distribution prior to the heating is retained in the velocity scaling. Third, we use an Eulerian description in which the pressure pulse moves in the MD cell frame of reference, whereas most other NEMD simulations of shock waves use a Lagrangian description in which the coordinate system moves with the shock [11, 35].

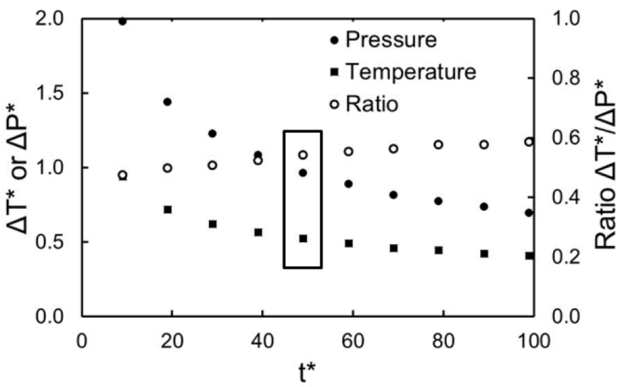

Fig. 9. Increase in temperature and pressure from equilibrium to peak values and the ratio between them. The framed points are from the same cases as shown in Figures 4 and 5

It is often assumed that a pressure wave is adiabatic. This raises the question of to what extent the thermal wave is a consequence of the pressure wave and a Joule-Thomson effect. Turning back to figures 4 and 5, we can quantify the ratio between the peak values of the pressure- and temperature waves relative to the equilibrium values in front of the wave as function of time (as the waves progress). The result is shown in Fig. 9. The plot also includes the ratio $\triangle T^*/\triangle P^*$, which in this case is of the order 0.4 – 0.6. The Joule-Thomson coefficient for three selected states near the wave front was computed from a series of equilibrium simulations, similarly to the speed-of-sound calculation and based on the expression

$$\mu = \frac{1}{C_P}\left[\left(\frac{\partial V}{\partial T}\right)_P T - V\right] \tag{15}$$

The following values were obtained: $\mu^* = 0.8,\ 0.2$, and 0.0 for the (equilibrium) state in front of the shock, in the steepest front of the pressure wave, and at the pressure peak, respectively. The Joule-Thomson coefficient can be positive or negative, depending on the thermodynamic state of the system. For a given temperature, the coefficient decreases and becomes negative with increasing pressure. We therefore did a simulation for the supercritical case (run 8), starting with equilibrium at $T^* = 3.0$ with a higher equilibrium pressure, for which the Joule-Thomson coefficient is expected to be negative.[4] The results are shown in Fig. 10. Also in this case, there is a local heating, whereas the Joule-Thomson effect would have given a local cooling if it were the dominant effect. The conclusion is that the Joule-Thomson effect contributes little or nothing to the heat wave.

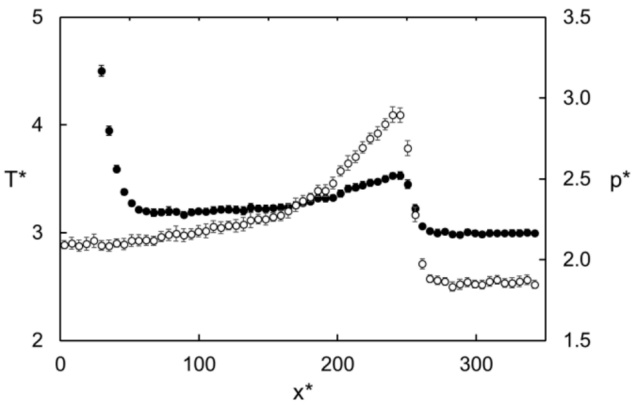

Fig. 10. Pressure- (white) and temperature (black) plots for a case where the Joule-Thomson coefficient is negative. Like for the other cases, the pressure wave causes a local heating

To examine the effect of pulsed *vs.* steady heat source, we did one simulation for the supercritical case with a pulsed source (run 4). The heat was turned on with the thermostat set point at $T^*_{\rm H} = 10.0$ and turned off at $t^*= 4$ and the system was then allowed to relax. The results for the pressure and temperature are shown in Fig. 11. The first observation from a comparison between Figures 4 and 11 is that the pressure wave travels with about the same speed in both cases. Secondly, like with the steady heat source, both the pressure and temperature stay at values higher than the equilibrium values in the region $75 < x^* < 125$, where the heat diffusion from the source has not yet reached at this time. The energy pumped into the system by the heat pulse is clearly dissipated by two quite different mechanisms; diffusion near the heat source and dissipation of the energy in the pressure wave.

In order to further examine the nature of the heat wave, we computed the local enthalpy in the system. Using the same supercritical snapshot at $t^*= 50$ as an example, the situation is shown in Fig. 12. Each layer is an open system that exchanges kinetic energy and enthalpy with the neighboring layers. In fact, at the peak of J^*_q (see Fig. 13), the numerical values of the first and second terms on the rhs of Eq. (10) are

[4] A more detailed analysis of the Joule-Thomson coefficient for the LJ/spline system will be presented in a forthcoming paper.

0.71 and 0.44, respectively. The prerequisite for an analysis in terms of the Joule-Thomson effect does not exist. This does not exclude that a Joule-Thomson effect contributes to the heat wave, but it is clearly not the only reason for it.

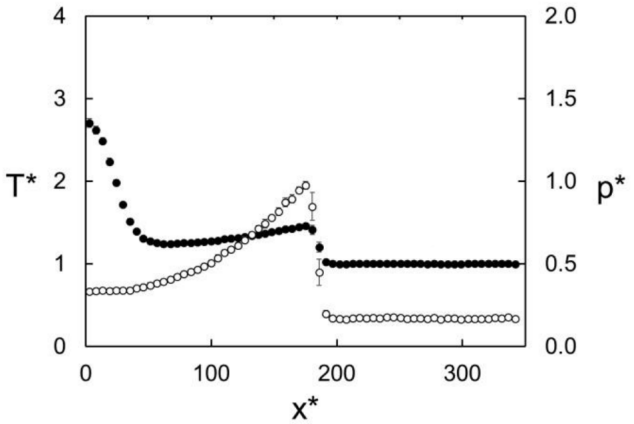

Fig. 11. Temperature- and pressure profiles at the same conditions as in Fig. 3, the supercritical case and at time $t^* = 50$ after the heat was turned on. Also in this case $T_H^* = 10.0$, but the heat source was switched off at $t^* = 4$. T_L^* was kept at 1.0. The uncertainties are shown as three standard deviations of the mean, based on 20 parallel runs

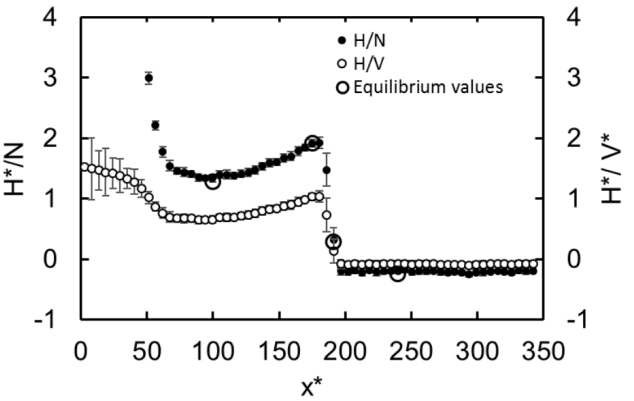

Fig. 12. Enthalpy per particle (black symbols) and enthalpy density (white circles) for the same case as shown in Fig. 4. The four larger circles are equilibrium values, see Section 3.4

III. 3. Fourier's law and the shock wave

We now turn to the question of the validity of Fourier's law in the shock wave. As already shown by the analysis of the heat dissipation near the heat source in terms of the heat equation, which implies Fourier's law, describes the situation well. On the other hand, Fig. 5 shows a region, $100 < x^* < 170$, where the temperature gradient is slightly positive. The corresponding heat flux shown in Fig. 13 is positive everywhere (or zero in the equilibrium region in front of the wave), indicating a violation of Fourier's law.

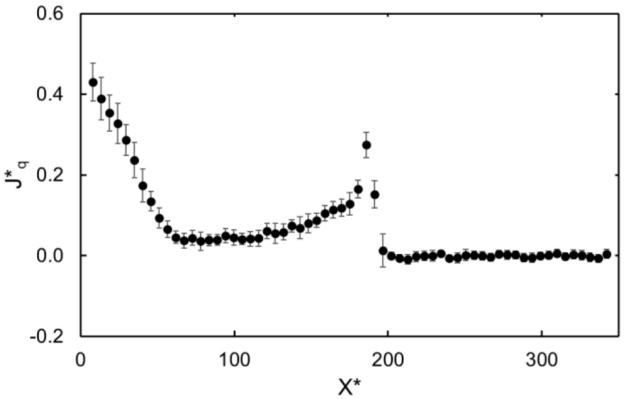

Fig. 13. Heat flux corresponding to the temperature profile in Fig. 5. Note that the heat flux is positive behind the shock wave, a region where the temperature gradient is also positive

The structure of the parabolic heat equation, Eq. (13) does not describe the wave. A thorough review of various models with hyperbolic equations was given by Joseph and Preziosi [27] and a comparison of results from the two types of equations was given by Vick and Özisik [36]. A particularly popular model for a hyperbolic heat equation that allows for a heat wave is the Cattaneo-Vernotte model [25, 26]. This model introduces the concept of a thermodynamic (or heat) relaxation time τ and reformulates the conservation law for heat as

$$J_{\mathrm{q}}(x,t) + \tau \frac{\partial J_{\mathrm{q}}(x,t)}{\partial t} = -k\nabla T(x,t), \qquad (16)$$

where k is the thermal conductivity. The idea is that the heat flux J_q is delayed a certain time τ in response to the force ∇T at time t and so it has a "memory" of the pulse. The NEMD simulations give us both the heat flux and the temperature gradient as function of x and t. The temperature gradient was computed with a five-point numerical differentiation of the temperature data, except near the shock front, where a three-point method was used.

The supercritical case is shown in Fig. 14 as function of time for the "window" at $x^* = 90$. We note that the heat flux after passage of the temperature front (the negative peak in ∇T) behaves as a typical relaxation. Approximating ∇T with a Dirac delta function, J_{q} is expected to show an exponential decay after passage of the peak [27],

$$J_{\mathrm{q}}(t) = \frac{k}{\tau}\exp\left(-\frac{t}{\tau}\right) \qquad (17)$$

This leads to the Cattaneo-Vernotte model, Eq. (16). Inspection of Fig. 14 shows that J_{q} does not relax to zero after the peak, so the model was modified to

$$J_{\mathrm{q}}(t) = J_\infty + \frac{k}{\tau}\exp\left(-\frac{t-t_0}{\tau}\right), \qquad (18)$$

where J_∞ is the level of the heat flux after a long time and t_0 is the time when the peak passes the "window". Using J_∞, k/τ, and τ as adjustable parameters in a least-squares regression gave the black line in Fig. 14 with estimates $J^*_\infty = 0.026$, $k^*/\tau^* = 0.44$, and $\tau^* = 6.6$. The value of t^*_0 was fixed at 19 as read from Fig. 14. Although the quality of the data does not allow for an accurate estimate for the thermal conductivity, the value deducted from the fit was $k^* \approx 2.9$. An independent estimate for k was obtained from a stationary-state NEMD run with $n^* = 0.5$ (approximate density at the peak), $T^*_{\mathrm{H}} = 1.6$, $T^*_{\mathrm{L}} = 1.4$, and a temperature gradient $\nabla T^* = -0.0125$, which gave $k^* = 2.96 \pm 0.04$. The good correspondence is probably by chance, but at least the two estimates for k are consistent. A better analysis will be required to resolve this.

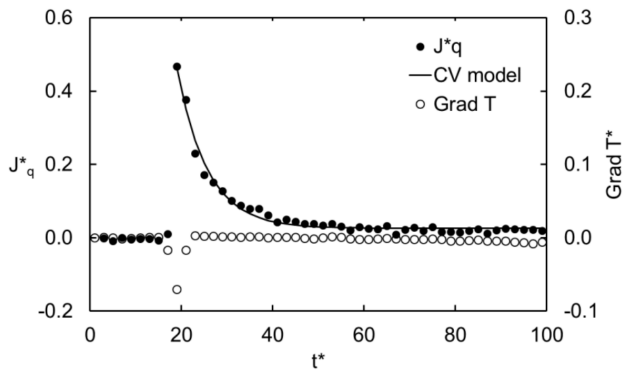

Fig. 14. Heat flux and temperature gradient as function of time for $x^* = 90$. The black line is the fit of Eq. (18) to the NEMD data for J^*_q. The gradient in T^* was calculated from a five-point numerical differentiation, except in the wave front and peak, where we used a three-point method

We conclude that the Cattaneo-Vernotte model does describe the observed transient heat flux quite well under the conditions in the present case.

III. 4. Local equilibrium

The last question we have addressed in this work, is that of local equilibrium. Based on our previous work [37], we have chosen to consider two indicators: (1) isotropy of the kinetic temperature and (2) the values of local thermodynamic properties in relation to the equilibrium equation-of-state values. The idea is that if one or both of these conditions are violated, local equilibrium is not fulfilled. The opposite case is a strong indication that local equilibrium is indeed fulfilled.

The kinetic temperature computed from Eq. (5) is a tensor. If the components of the tensor are equal, the temperature may be considered to be isotropic. Fig. 15 shows that this is the case, which is not consistent with previous studies of shock waves, except the work by Guo *et. al.* [38]. We also found that the pressure is isotropic even in the shock wave (not shown here), another indication of local equilibrium. The dense gas case showed a slight difference between the temperature components, whereas the difference in the dilue gas was more pronounced as shown in Fig. 16.

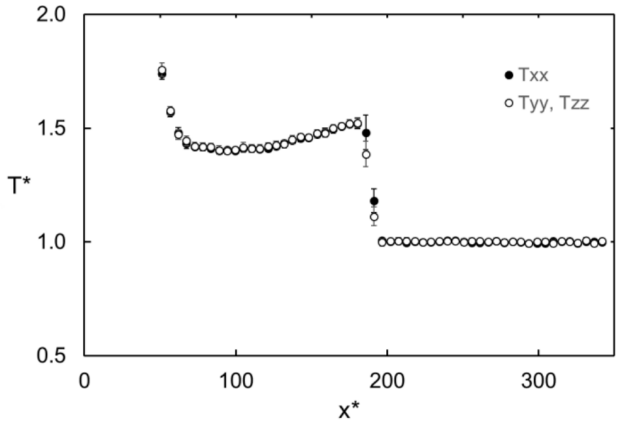

Fig. 15. Local temperature tensor components at $t^* = 50$ for the supercritical case

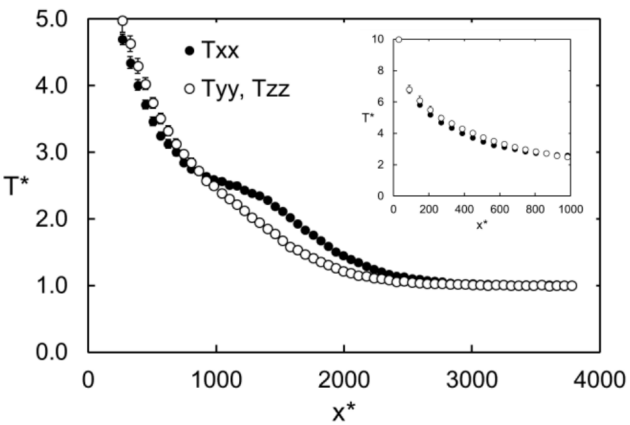

Fig. 16. Local temperature tensor components at $t^* = 400$ from the non-equilibrium simulation in the dilute-gas case, run 10 ($n^* = 0.001$). For this state, the system obeys the ideal-gas law, $Z = 1.0$. The total number of particles was 432,000 in this case (see also Table II). Note the lack of isotropy in the range $1000 < x^* < 2000$

The other check on local equilibrium was based on comparing the local equation of state in the transient case with results from equilibrium simulations. Four state point were chosen from the non-equilibrium simulation. As an example, the supercritical case at $t^* = 50$ is included here. Equilibrium NVT-simulations were done with $N = 4096$, the selected densities and temperatures as input, and the corresponding pressure and enthalpy were computed. The comparison is shown as the four large, white circles in Fig. 4 for the pressure and Fig. 12 for the enthalpy. These comparisons also show that the local equilibrium condition is not violated. Equally close similarity between non-equilibrium and equilibrium results were found also in the liquid and dense gas cases.

IV. DISCUSSION

The results presented here answer some of the questions raised in the introduction, but leave some others unsolved. The heat wave associated with the pressure wave may have a contribution from the Joule-Thomson effect, but the effect must be small in the case examined in detail here. Runs 3 and 8 represent equilibrium states with opposite signs for the Joule-Thomson coefficient, yet the pressure wave heats up the system with about the same ratio $\triangle T^*/\triangle P^* \sim 0.5$ in both cases at $t^* = 50$. The work presented here is (by chance) very similar to the work by Guo *et. al.* [38], which has not received much attention in the literature. Guo *et. al.* used a pulsed heat source in an otherwise very similar set-up compared with what we have used. They also found propagating waves of pressure and temperature. However, they found that the pressure and temperature resumed the equilibrium values after the wave had passed. For such a reversible, adiabatic process the Joule-Thomson effect should be responsible for the coupling between the pressure and the temperature, a conjecture we cannot confirm. Guo *et. al.* point at an apparent disagreement with some previous NEMD simulations for a 2D system on liquid argon [39]. It seems that ref [39] reports a temperature wave in agreement with the CV model whereas ref [38] does not.

Another approach is to follow arguments of Boukari *et. al.* [40], leading to the relation

$$\frac{dT}{dP} = \frac{1}{\beta}\left(\alpha_T - \frac{d\ln n}{dP}\right) \tag{19}$$

where α_T is the isothermal compressibility and β is the volume expansion coefficient. This gives $\triangle T^*/\triangle P^* \sim 1$ for run 3 at $t^* = 50$, which is not in agreement with the observed effect. The estimates based on the Joule-Thomson effect and Eq. (19) do not take into account viscous dissipation of the energy or heat diffusion caused by the temperature gradients near the shock front. Fig. 13 shows a strong heat flux in the shock front, leading energy away from the pressure peak and so reducing the temperature. This effect is not taken into account in the effects discussed above. Another effect which is omitted in the analysis is the viscous dissipation of energy due to the bulk viscosity. There is no shear in the system, but the compression of the fluid by the pressure wave will lead to viscous forces. This effect, and the role of the entropy production in the shock wave, including the thermoacoustic effect discussed by Onuki [41] will be topic of a forthcoming paper.

It seems clear that the heat diffusion near the heat source is consistent with the heat equation, which implies Fourier's law. It is somewhat surprising that a constant value of the thermal diffusivity works over such a wide range of temperature and density as shown here, although this has also been observed in our previous works [30, 37] . On the other hand, Fourier's law does not seem to work in (and behind) the shock wave, where we found that the Cattaneo-Vernotte model describes the heat conservation quite well. However, the estimated value for the thermodynamic relaxation time does not completely remove the apparent disagreement between the positive gradients in both J_q and ∇T behind the shock wave when the term $\tau\partial J_\mathrm{q}/\partial t$ is added in the Cattaneo-Vernotte model, but this question will also require a more robust analysis of the data, especially of the numerical differentiation methods used here.

Very surprisingly, there are strong indications that the system is in local equilibrium in the shock wave. This is quite controversial, as all previous NEMD studies (except Guo *et. al.* [38]) have shown that this is not the case. The exception found in the present work was for the dilute gas, where the temperature was found to be slightly non-isotropic, but not at all the same anisotropy as found in previous studies. This is not a question of density as previous studies have also included liquids. It may be a consequence of the way the shock wave was generated, because the traditional virtual piston creates a velocity distribution that is highly non-isotropic.

Our results do not support the idea that the success of the Cattaneo-Vernotte model is in conflict with the local-equilibrium assumption in classical irreversible thermodynamics and the need to go to extended irreversible thermodynamics [42]. On the contrary, our results are consistent with local equilibrium in the shock wave as well as the Cattaneo - Vernotte model giving a reasonably good description of the heat flux associated with the shock wave. This supports the arguments by Glavatsky that the heat transport may well be analyzed in terms of the local equilibrium assumption [43].

Another disagreement with previous studies is the thickness of the shock wave. We find that the thickness is of the order 15 σ both in the supercritical and liquid cases, whereas it was previously found to be 2 – 3 σ [35]. This discrepancy may also be related to how the shock wave was generated and the velocity distribution in the shock front.

V. CONCLUSIONS

The main conclusion from the present work is that the Fourier's law is violated in a thermal shock wave associated with a pressure shock caused by a sudden thermal explosion. The heat wave is not due to the Joule-Thomson effect, at least not exclusively, as seen from the fact that the fluid heats up in a state where the Joule-Thomson effect should lead to cooling down. We found that the Cattaneo-Vernotte model describes the heat flux behind the shock wave quite well and gives consistent values for the thermal conductivity. The indicators for local equilibrium used here show that the system is in local equilibrium, even in the shock wave, except in the ideal-gas case. This allows the data to be analysed in terms of irreversible thermodynamics.

Appendix A. The thermostat.

The velocity scaling was applied to the particles in the thermostatted layers by setting

$$\mathbf{v}_i^{\mathrm{new}} = a\mathbf{v}_i^{\mathrm{old}} + \boldsymbol{\beta}, \tag{A1}$$

where $\mathbf{v}_i^{\mathrm{old}}$ and $\mathbf{v}_i^{\mathrm{new}}$ are the velocity of particle *i* before and after scaling, respectively, a is a scaling factor, and $\boldsymbol{\beta}$ is a vector that adjusts the particles' momenta. Suppose the total momentum of the particles in layer l after scaling is

$$\mathbf{P}^{\mathrm{new}} = m\sum_{i\in l}\mathbf{v}_i^{\mathrm{new}} \tag{A2}$$

and likewise for $\mathbf{P}^{\mathrm{old}}$. The change in momentum with the scaling, and the conservation of momentum gives

$$\triangle\mathbf{P} = \mathbf{P}^{\mathrm{new}} - \mathbf{P}^{\mathrm{old}} = 0 \tag{A3}$$

Momentum for the particles in the non-thermostated layers is conserved by the equations of motion.

Inserting Eq. (A1) into (A2) and using (A3) gives

$$\boldsymbol{\beta} = \frac{1-a}{N_l}\sum_{i\in l}\mathbf{v}_i^{\mathrm{old}} \tag{A3}$$

The kinetic energy in layer l after scaling is

$$e_{\mathrm{kinetic}}^{\mathrm{new}} = \frac{m}{2}\sum_{i\in l}(\mathbf{v}_i^{\mathrm{new}})^2 \tag{A5}$$

Inserting Eq. (A1) into (A4) and expressing the new kinetic energy in terms of the thermostat set point T^{set} gives

$$\begin{aligned}&\frac{3}{2}N_l k_{\mathrm{B}}T^{\mathrm{set}} = e_{\mathrm{kinetic}}^{\mathrm{new}} = \\ =&\frac{m}{2}\left[a^2\sum_{i\in l}\left(\mathbf{v}_i^{\mathrm{old}}\right)^2 + 2a\sum_{i\in l}\boldsymbol{\beta}\cdot\mathbf{v}_i^{\mathrm{old}} + N_l\boldsymbol{\beta}^2\right]\end{aligned} \tag{A6}$$

Eq. (A6) is a quadratic equation in a. The solution is then used with Eq. (A4) to update the velocities.

This algorithm is in principle the same as the HEX algorithm [24], but whereas we here specify T^{set}, the HEX algorithm is based on specifying the change in kinetic energy, $e_{\mathrm{kinetic}}^{\mathrm{new}} - e_{\mathrm{kinetic}}^{\mathrm{old}}$.

The quadratic equation in a does not always have a real solution, in which case the thermostatting attempt is skipped and the old velocities are used without change.

Appendix B. Computation of the speed of sound

The speed of sound at zero frequency, v_s, in a fluid is given by [9]

$$v_s^2 = \left(\frac{\partial P}{\partial\rho}\right)_S = \gamma\left(\frac{\partial P}{\partial\rho}\right)_T \tag{B1}$$

where γ is the heat capacity ratio, $\gamma = C_P/C_V$.

The inverse isothermal compressibility was computed as follows: For each of the investigated states (gas, supercritical, and liquid), a series of four equilibrium NVT-simulations were made at the equilibrium temperature (in front of the shock wave) and four different densities. In each case, $N = 8000$. The same NEMD code with the same thermostatting method that was used in the non-equilibrium simulations was also used here, except that the MD-cell aspect ratio was 2:1 and divided into 64 layers. The thermostat set points were equal to the equilibrium temperature of interest. Each run was started from an fcc-configuration and 1,000,000 Monte Carlo steps to equilibrate the system, followed by 4,000,000 MD steps where the last 2,000,000 steps were used to get the equilibrium data. Only the non-thermostatted layers in the MD cell were used for acquisition of thermodynamic properties. The four runs were carried out with slightly different number densities, and the slope was determined from a linear fit to the data for P^* *vs.* n^*.

The heat capacity at constant volume was determined from a series of four equilibrium runs, similar to the determination of the isothermal compressibility, except that the temperature was varied instead of the volume.

The heat capacity at constant pressure could have been determined in a similar way from a NPT-simulation. Instead, we did a series of four non-equilibrium runs, making use of the observation that local equilibrium is well achieved in a non-equilibrium simulation [37]. This means that if the pressure is uniform across the system, equilibrium properties at constant pressure may be computed from a single NEMD run. This procedure has a minor cost. In the NEMD simulation, only the overall density and the thermostat set points are fixed. The local values are a priori undetermined and known only when the simulation is finished. This means that if the thermodynamic state of interest is given by *e.g.* the temperature and density, a series of NEMD runs that cover the range of interest must be made.

Results from these simulations are shown in Tab. B1 for the supercritical state. From these data, the speed of sound can be calculated as

$$v_s^* = \sqrt{\frac{C_P^*}{C_V^*}\left(\frac{\partial P^*}{\partial n^*}\right)_{T^*}} = \sqrt{\frac{14.22}{2.56}\times 0.39} = 1.47 \tag{B2}$$

Tab. B1. Results for the computation of the speed of sound in the supercritical state

n^*_{overall}	T^*	P^*	n^*	$(\partial P^*/\partial n^*)_{T^*}$
0.36	1.00	0.155	0.36	
0.38	1.00	0.161	0.38	
	1.00	0.163	0.40	**0.390**
0.42	1.00	0.177	0.42	
0.44	1.00	0.186	0.44	

n^*_{overall}	T^*	P^*	n^*	$u^* = U/(N\epsilon)$	C^*_V
0.4	0.980	0.153	0.400	-0.683	
0.4	0.990	0.159	0.400	-0.659	
	0.991	0.163	0.400	-0.653	**2.56**
0.4	1.01	0.177	0.400	-0.606	
0.4	1.02	0.185	0.400	-0.581	

T^*_{H}	T^*_{L}	n^*	P^*	C^*_P
1.01	0.95	0.4	0.151	15.41
1.02	0.96	0.4	0.161	14.36
		0.4	0.163	**14.22**
1.04	0.98	0.4	0.177	12.91
1.05	0.99	0.4	0.185	12.05

Acknowledgements

This work started as a project with students Sebastian Wolf and Donato Maria Mancino, with whom I had interesting discussions during problem formulation. Good discussions with Dick Bedeaux, Signe Kjelstrup, Akira Onuki, Lin Chen, and Tamio Ikeshoji were also highly appreciated. Computer resources have been provided by Faculty of Natural Sciences and Technology at NTNU and by the HPC resources at UiT provided by NOTUR, http://www.sigma2.no.

References

[1] B.J. Alder and T. Wainwright, *Phase Transition for a Hard Sphere System,* J. Chem. Phys. **27**, pp. 1208–1209, 1959.

[2] W.G. Hoover, *Nonequilibrium Molecular Dynamics,* Ann. Rev. Phys. Chem. **34**, pp. 103–127, 1983.

[3] R.K. Eckhoff, *Water vapour explosions - A brief review,* J. Loss Prevention in the Process Industries **40**, pp. 188–198, 2016.

[4] L.A. Dombrovsky, *Steam explosions in nuclear reactors: Droplets of molten steel vs core melt droplets,* Int. J. Heat and Mass Transfer **107**, pp. 432–438, 2017.

[5] Y. Liu, T. Olewski and L. N. Véchot, *Modeling of a cryogenic liquid pool boiling by CFD simulation,* J. Loss Prevention in the Process Industries **35**, pp. 125–134, 2015.

[6] K.A. Bhaskaran and P. Roth, *The shock tube as wave reactor for kinetic studies and material systems,* Progress in energy and combustion science **28**, pp. 151–192, 2002.

[7] K. Thoma, U. Hornemann, M. Sauer and E. Schneider, *Shock waves - Phenomenology, experimental, and numerical simulation,* Meteorites & Planetary Science **40**, pp. 1283–1298, 2005.

[8] L.D. Landau and E. M. Lifshitz, Fluid Mechanics, Oxford: Pergamon Press, 1959.

[9] J.O. Hirschfelder, C. F. Curtiss and R. B. Bird, Molecular theory of Gases and Liquids, New York: John Wiley & Sons, 1954.

[10] W.G. Hoover and C. G. Hoover, Simulations and Control of Chaotic Nonequilibrium Systems, Advanced Series in Nonlinear Dynamics, Vol 27, New Jersey: World Scientific, 2015.

[11] W.G. Hoover, *Structure of a Shock-Wave Front in a Liquid,* Phys. Rev. Lett. **42**, pp. 1531–1534, 1979.

[12] W.G. Hoover, H. C. G. and F. J. Uribe, *Flexible Macroscopic Models for Dense-Fluid Shockwaves: Partitioning Heat and Work; Delaying Stress and Heat Flux; Two-Temperature Thermal Relaxation,* arcXiv, p. 1005.1525v1, 2010.

[13] W.G. Hoover and C. G. Hoover, *Tensor Temperature and Shock-wave Stability in a Strong Two-Dimensional Shockwave,* arcXiv, p. 0905.1913v2, 2013.

[14] W.G. Hoover, C. G. Hoover and K. Travis, *Shock-Wave Compression and Joule-Thomson Expansion,* Phys. Rev. Lett. **112**, p. 144504, 2014.

[15] B.L. Holian, *Atomistic computer simulations of shock waves,* Shock Waves **5**, pp. 149–157, 1995.

[16] B.L. Holian and M. Mareschal, *Heat-flow equation motivated by the ideal-gas shock wave,* Phys. Rev. E **82**, p. 026707, 2010.

[17] D.-S. Tang, Y.-C. Hua, B.-D. Nie and B.-Y. Cao, *Phonon wave propagation in ballistic-diffusive regime,* J. Applied Phys. **119**, p. 124301, 2016.

[18] B.L. Holian, W. G. Hoover, B. Moran and G. K. Straub, *Shock-wave structure via nonequilibrium molecular dynamics and Navier-Stokes continuum mechanics,* Phys. Rev. A **22**, pp. 2798–2808, 1980.

[19] W.J. M. Rankine, *On the thermodynamic theory of waves of finite longitudinal distrubances,* Phil. Trans. Roy. Soc. London **160**, pp. 277–288, 1870.

[20] H. Hugoniot, *Mémoire sur la propagation des mouvements dans les corps et spécialement dans les gaz parfaits (premičre partie),* J. École Polytechnique **58**, pp. 1–125, 1887.

[21] B. Zappoli, D. Beysens and Y. Garrabos, Heat Transfers and Related Effects in Supercritical Fluids, London: Springer, 2015.

[22] L. Chen, Microchannel Flow Dynamics and Heat Transfer of Near-Critical Fluid, Singapore: Springer, 2017.
[23] A. Onuki, H. Hao and R. A. Ferrell, *Fast adiabatic equilibration in a single-component fluid near the liquid-vapor critical point,* Phys. Rev. A **41**, pp. 2256–2259, 1990.
[24] T. Ikeshoji and B. Hafskjold, *Non-equilibrium molecular dynamics calculation of heat conduction in liquid and through liquid-gas interface,* Mol. Phys. **81**, pp. 251–261, 1994.
[25] C. Cattaneo, *Sulla conduzione del calore,* Atti del Semin. Mat. e Fis. Uni. Modena **3**, pp. 83–101, 1948.
[26] P. Vernotte, *Les paradoxes de la théorie continue de l'équation de la chaleur,* C. R. Hebd. Sceances Acad. Sci. **246**, pp. 3154–3155, 1958.
[27] D. D. Joseph and L. Preziosi, *Heat waves,* Rev. Mod. Phys. **61**, pp. 41–73, 1989.
[28] B.L. Holian and D. J. Evans, *Shear viscosities away from the melting line: A comparison of equilibrium and nonequilibrium molecular dynamics,* J. Chem. Phys. **78**, pp. 5147–5150, 1983.
[29] D.M. Heyes, *The Lennard-Jones Fluid i the Liquid-Vapour Region,* CMST **21**, no. 4, pp. 169–179, 2015.
[30] B. Hafskjold, T. Ikeshoji and S. K. Ratkje, *On the molecular mechanism of thermal diffusion in liquids,* Mol. Phys. **80**, pp. 1389–1412, 1993.
[31] S. Kjelstrup, D. Bedeaux, E. Johannesen and J. Gross, Non-Equilibrium Thermodynamics for Engineers, New Jersey: World Scientific, 2010.
[32] D. J. Evans and G. P. Morriss, Statistical Mechanics of Nonequilibrium Liquids, Canberra: ANU E Press, 2007.
[33] Y. Huang and H. H. Bau, *Thermoacoustic waves in a semi-infinite medium,* Int. J. Heat and Mass Transfer **38**, no. 8, pp. 1329–1345, 1995.
[34] A. Nakano, *Studies on piston and soret effects in a binary mixture supercritical fluid,* Int. J. Heat and Mass Transfer **50**, pp. 4678–4687, 2007.
[35] B. L. Holian, *Modeling shock-wave deformation via molecular dynamics,* Phys. Rev. A **37**, pp. 2562–2568, 1988.
[36] B. Vick and M. N. Özisik, *Growth and Decay of a Thermal Pulse Predicted by the Hyperbolic Heat Conduction Equation,* Trans. ASME **105**, pp. 902–907, 1983.
[37] B. Hafskjold and S. K. Ratkje, *Criteria for Local Equilibrium in a System with Transport of Heat and Mass,* J. Stat. Phys. **78**, pp. 463–494, 1995.
[38] Y.-K. Guo, Z.-Y. Guo and X.-G. Liang, *Three-Dimensional Molecular Dynamics Simulation on Heat Propagation in Liquid Argon,* Chin. Phys. Lett. **18**, pp. 71–73, 2001.
[39] Z. Guo, D. Xiong and Z. Li, *Molecular Dynamics Simulation of Heat Propagation in Liquid Argon,* Tsinghua Sci. Tech. **2**, no. 2, pp. 613–618, 1997.
[40] H. Boukari, J. N. Shaumeyer, M. E. Briggs and R. W. Gammon, *Critical speeding up in pure fluids,* Phys. Rev. A **41**, no. 4, pp. 2260–2263, 1990.
[41] A. Onuki, *Thermoacoustic effects in supercritical fluids near the critical point: Resonance, piston effect, and acoustic emission and reflection,* Phys. Rev. E **76**, p. 061126, 2007.
[42] G. Lebon and D. Jou, *Early history of extended irreversible termodynamics (1953–1983): An exploration beyond local equilibrium and classical transport theory,* Eur. Phys. J. H **40**, pp. 205–240, 2015.
[43] K. S. Glavatsky, *Local equilibrium and the second law of thermodynamics for irreversible systems with thermodynamic inertia,* J. Chem. Phys. **143**, pp. 164101-1–11, 2015.6

Bjørn Hafskjold, Dr. Techn., graduated from the Norwegian Institute of Technology in 1971 and received his doctorate degree from the same university in 1979. He is now professor in Physical Chemistry at the Norwegian University of Science and Technology (NTNU). His main scientific topic is computer simulations of thermodynamic and transport properties of fluids, but he has also worked on oil/water/gas separator design and operation, modelling of hydrocarbon mixtures, and experimental determination of phase equilibria at high pressure. He has international experience from contract research for international oil companies, from stays in USA, France, England, and Japan. He has published more than 70 scientific papers in international journals plus numerous technical reports and conference presentations. Hafskjold has extensive administrative experience from serving as Dean at the Norwegian University of Science and Technology (NTNU), Director of the Norwegian high-performance computing project NOTUR, and other projects. He is member of the Norwegian Academy of Technological Sciences.